

See discussions, stats, and author profiles for this publication at: <https://www.researchgate.net/publication/26746998>

Theoretical and Experimental Study of Negative LiF Clusters Produced by Fast Ion Impact on a Polycrystalline (LiF)-Li-7 Target

ARTICLE in THE JOURNAL OF PHYSICAL CHEMISTRY A · SEPTEMBER 2009

Impact Factor: 2.69 · DOI: 10.1021/jp905138d · Source: PubMed

CITATIONS

12

READS

35

7 AUTHORS, INCLUDING:



André S Pimentel

Pontifícia Universidade Católica do Rio de Janeiro

46 PUBLICATIONS 370 CITATIONS

[SEE PROFILE](#)



Marco Aurélio Cavalcanti Pacheco

Pontifícia Universidade Católica do Rio de Janeiro

172 PUBLICATIONS 1,396 CITATIONS

[SEE PROFILE](#)



Marco Nascimento

Federal University of Rio de Janeiro

143 PUBLICATIONS 1,914 CITATIONS

[SEE PROFILE](#)



Enio Frota da Silveira

Pontifícia Universidade Católica do Rio de Janeiro

179 PUBLICATIONS 1,173 CITATIONS

[SEE PROFILE](#)

Theoretical and Experimental Study of Negative LiF Clusters Produced by Fast Ion Impact on a Polycrystalline ^7LiF Target[†]

Francisco Alberto Fernandez-Lima,[‡] Omar P. Vilela Neto,[§] André Silva Pimentel,^{||} M. A. C. Pacheco,[§] Cássia Ribeiro Ponciano,[⊥] Marco Antonio Chaer Nascimento,[#] and E. F. da Silveira^{*,⊥}

Chemistry Department, Texas A&M University, College Station, TX, Electrical Engineering, Chemistry, and Physics Departments, Pontifícia Universidade Católica, Rio de Janeiro, Brazil, and Chemistry Institute, Universidade Federal do Rio de Janeiro, Rio de Janeiro, Brazil

Received: June 1, 2009; Revised Manuscript Received: July 13, 2009

The emission of negative cluster ions produced by the impact of ~ 60 MeV ^{252}Cf fission fragments on a ^7LiF polycrystalline target is analyzed. The negative ion mass spectrum is dominated by the $(^7\text{LiF})_n\text{F}^-$ series, $n = 1$ to ~ 30 . The desorption yield distribution of the $(^7\text{LiF})_n\text{F}^-$ members has a maximum at $n = 2$ and then decreases as the sum of two exponentials whose decay parameters are $k_{\text{fast}} = 0.9$ and $k_{\text{slow}} = 0.08$. These k values are the same as those observed for the positive series and close to others obtained for condensed gas targets. Relative cluster ion stabilities, deduced from the experimental ion abundances for the $(\text{LiF})_n\text{F}^-$ series, are proposed to be correlated with theoretical structures according to their internal energy by using the deviation plot (D-plot) methodology. A pool of candidate cluster structures was generated using a genetic algorithm and further analyzed and optimized using density functional theory (DFT) with the hybrid functional B3LYP (DFT/B3LYP) and Möller-Plesset perturbation theory (MP2). For the small clusters ($n = 1$ to 2), the most stable structures are found to be linear, whereas the larger clusters ($n = 4$ to 6) present cubic or polyhedral structures. Fragmentation energies, ionization potentials, and relative stabilities are reported for the most abundant families of the $(\text{LiF})_n\text{F}^-$ and $(\text{LiF})_n^-$ series.

1. Introduction

The bombardment of solids by fast projectiles produces a number of desorbed/sputtered species whose yield depends on the projectile characteristics (energy, charge state, cluster structure) as well as on those of the secondary particle. The desorbed/sputtered species are mainly neutral, and only a small portion corresponds to secondary ions (SIs). For alkali halide targets, relatively high desorption yields of SI are expected because of the ionic nature of the material. Most of the previous studies have been focused on the emission of positive SIs by ion bombardment. Nevertheless, the analysis of negative SIs is also important not only as a contribution to the understanding of the fundamental nature of the SI emission process but also because of their distinctive potential as generators of negative primary ion beams for practical applications. In particular, negative ion beams are suitable (i) for low-energy (electronvolts to kiloelectronvolts) charge-exchange experiments with surfaces,¹ (ii) as a source to sputter ions for positive ion sources,² and (iii) for injecting negative ion beams into electrostatic tandem accelerators.³ For cluster ion projectiles, it is well known that they are capable of inducing much higher desorption yields than atomic ions projectiles and are therefore suitable for surface analysis, erosion devices, and beam sources for secondary ion mass spectrometry (SIMS).^{4–7}

The dependence of the negative SI abundances on the beam parameters has been studied by a number of researchers. For example, Michiels and Gijbels reported a comparison of negative SI mass spectra of fluoride salts by laser ablation and SIMS but did not advance any conclusions about the nature of emission mechanisms.⁸ Standing et al. measured negative SI spectra from various alkali halides using 11 to 28 keV alkali projectiles; the ratios of cluster desorption yields were found to be independent of the primary ion energy loss, and a recombination model was discussed.⁹ Twu et al.¹⁰ reported mass spectra of positive and negative cluster ions produced by laser vaporization of alkali halide targets. They observed very similar mass spectra shapes and concluded that except for the NaI target, the observed magic numbers indicate the existence of surface terraces, mostly connected to the cubicle nature of the lattice.¹⁰

Schweikert and coworkers have employed $(\text{CsI})_n\text{I}^-$ negative cluster ions as kiloelectronvolt projectiles for surface characterization and luminescence studies.^{11,12} Li et al. have studied the surface fragmentation process using photon-stimulated ejection of atoms from alkali halide nanocrystals.¹³ Betz and Wien¹⁴ reviewed the energy and angular distributions of sputtered particles from alkali halide targets and proposed, for the CsI target, that particle emission occurs via the decay into ion pairs: $(\text{CsI})_m^* \rightarrow (\text{CsI})_n\text{Cs}^+ + (\text{CsI})_{m-n}\text{I}^-$.

In 1997, a series of experiments was performed by Pereira et al. aiming to understand the mechanism of LiF sputtering by MeV projectiles.^{15–17} Secondary positive and negative cluster ions were identified by time-of-flight (TOF), and their initial energy distributions were determined for several projectile energies. Unexpectedly, the results showed the coexistence of multiple emission mechanisms: the Li^+ and $(\text{LiF})\text{Li}^+$ ion emission is based on the projectile-target electron interaction,

[†] Part of the “Vincenzo Aquilanti Festschrift”.

* Corresponding author. Tel.: 55-21-35271272. Fax: 55-21-35271040. E-mail: enio@vlg.fis.puc-rio.br.

[‡] Texas A&M University.

[§] Electrical Engineering Department, Pontifícia Universidade Católica.

^{||} Chemistry Department, Pontifícia Universidade Católica.

[⊥] Physics Department, Pontifícia Universidade Católica.

[#] Universidade Federal do Rio de Janeiro.

whereas the F^- emission depends on the projectile–target nucleus interaction. Toulemonde et al. irradiated LiF single crystals by 1 MeV/u swift heavy ions and found that the LiF emission presents a very high secondary yield of neutrals ($\sim 10^4$ atoms/ion), and an angular distribution exhibiting an anisotropic jetlike component peaked normal to the sample surface, overlapping an isotropic component.^{18,19} Higher projectile energies or ion charges were used by Lenoir et al., who bombarded a LiF crystal with Ca^{17+} (9 MeV/u) and Xe^{21+} (17 keV/q = 350 keV) ions and reported different energy distributions for each system: the material responds differently to electronic interaction transfer (high-velocity projectiles) and to slow highly charged ion interaction.²⁰

In a different approach, Ponciano et al.^{21,22} showed that polycrystalline LiF targets bombarded by heavy ions emit cluster ions in excited states, which decay in-flight with lifetimes up to hundreds of nanoseconds after the impact. The $(LiF)_nLi^+$ emitted ions were analyzed by a TOF reflectron mass spectrometer, allowing coincidence measurements of neutral and ionic fragments of the precursor parent cluster ion. It was observed that a considerable fraction of positive cluster ions is emitted in excited states, suggesting that the same could occur with neutral or negative ion secondary clusters. Recently, Moria and Hiraoka employed electrospray droplet impact on alkali halide targets to produce positive and negative cluster ions.²³ The population distribution of negative cluster ions, $(XY)_nY^-$, has been observed to be narrower than that for positive cluster ions, $(XY)_nX^+$, a result that the authors attributed to the fact that the mutual Coulombic repulsion between the larger-sized halides causes a higher stability than the alkali ions. Moreover, they found a particularly low production yield of fluoride cluster ions $(XF)_nF^-$.

The variety of properties exhibited by LiF SI emission responds to such a complex emission mechanism. In a recent paper,²⁴ we described the emission of positive LiF clusters produced by fast ion impact on a polycrystalline LiF target. DFT calculations were reported for these clusters, and their relative SI abundances were correlated with the relative stability of the clusters structure.²⁴

In the present work, we extend this analysis to the negative $(LiF)_nF^-$ and $(LiF)_n^-$ clusters series. New experimental data for negative SIs produced by ~ 60 MeV ^{252}Cf fission fragments on a polycrystalline 7LiF target are presented. Candidate structures for the $(LiF)_nF^-$ series are obtained out of a “pool” of structures generated by a genetic algorithm (GA) and further optimized using density functional theory (DFT) with the hybrid functional B3LYP (DFT/B3LYP) and Möller-Plesset perturbation theory (MP2). An energy criterion is employed for a proper taxonomic description of the optimized cluster isomers (D-plot methodology). Cluster ion properties such as fragmentation energy, ionization potential, and relative stability are reported for the proposed structures. To the best of our knowledge, this is the first investigation to characterize the structures of the $(LiF)_nF^-$ and $(LiF)_n^-$ series.

2. Experimental Approach

Plasma desorption mass spectrometry (PDMS) was used to study the negative SIs emitted from a polycrystalline LiF target when bombarded by ~ 60 MeV ^{252}Cf fission fragments (FF). A ~ 100 nm thick 99% 7Li enriched LiF layer was deposited onto a thin Al foil by evaporation. Details of the experimental setup and of this technique are described in previous publications.^{22,24} A ^{252}Cf source continuously emits pairs of fission fragments; one of them is detected by a microchannel plate detector (MCP)

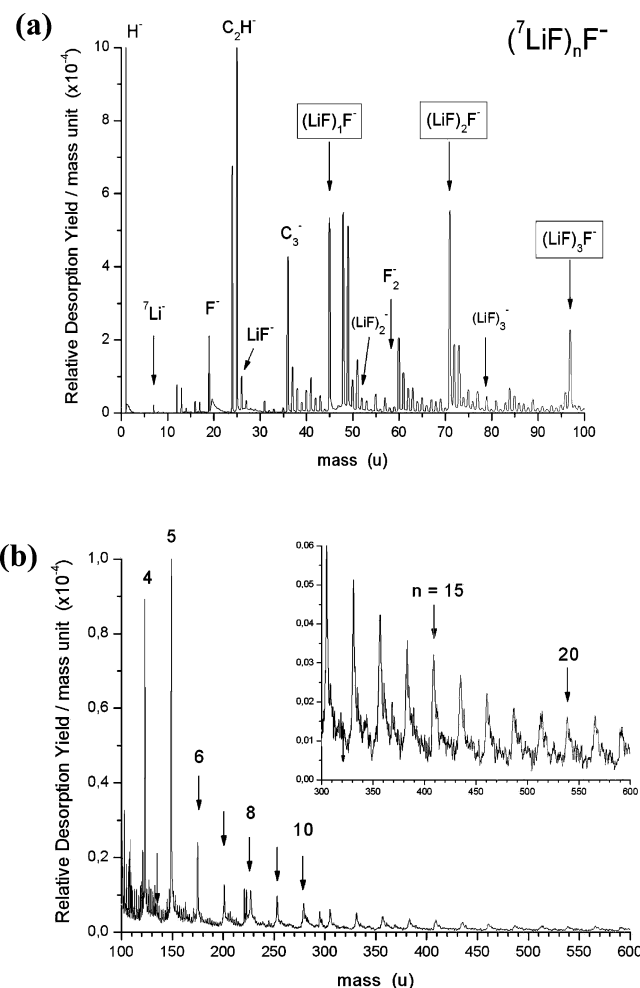


Figure 1. PDMS-TOF spectrum of the negative secondary ions from a 99% isotopically enriched 7Li polycrystalline LiF target: (a) 0–100 u mass range and (b) 100–600 u mass range. $(LiF)_nF^-$ members have smaller desorption yields than those of $(LiF)_nF^-$.

and used as a TOF “start” signal, whereas the second one traverses the thin Al foil support and a ~ 100 nm thick layer of 7LiF . The desorbed ions are accelerated by the extraction field toward the drift region and are detected by a second MCP, which delivers the corresponding TOF “stop” signal. Start and stop signals are used in a digital clock to determine the time-of-flight (TOF) of the individual secondary ions.

The extraction potential was 12 kV, and the residual gas pressure was lower than 10^{-6} mbar. The obtained PDMS negative ion spectrum of the evaporated LiF is presented in Figure 1, where peaks of the $(^7LiF)_nF^-$ series can be observed up to $n \approx 30$. Because the corresponding desorption yields at low masses are comparable to the background, the spectrum of the Al substrate was also obtained for correction. This is particularly important for the analysis of the $(^7LiF)_nF^-$ series yields, which are at least one order of magnitude lower than those of the $(^7LiF)_nF^-$ ions. Besides the LiF series members, the peaks in the mass spectrum relative to masses 7, 8, 14, 31, 38, 39, and 57 u are attributed to Li^- , LiH^- , Li_2^- , CF^- , F_2^- , HF_2^- , and F_3^- , whereas those corresponding to mass 1, 16, and 17 u are attributed to H^- , O^- , and OH^- , respectively. The peaks relative to the masses 24/25, 36/37, 48/49 u, and so on are presumably due to the vapor oil fragments and correspond to C_n^-/C_nH^- cluster ion series. The broad structures or peak tails at the right side of each high peak are produced by delayed emission sputtering.²²

3. Theoretical and Computational Approach

A pool of candidate structures for the negative cluster ions with $n \leq 5$ is first generated using a GA, described below. These structures are further optimized at the DFT/B3LYP and MP2 levels of theory. The D-plot methodology is then used to classify the optimized structures, and the relative stability of the isomers is compared with the experiments. Fragmentation energies and ionization potentials for the clusters are also computed.

3.1. Search for Stable Configurations: The Genetic Algorithm. The GA is an optimization and search technique based on the principle of nature evolution. A detailed description of the GA can be found elsewhere.²⁵ The search for the cluster geometries strongly depends on the choice of the initial structures regardless of the theoretical method. For that reason, over the last several years, GAs have been proposed to improve the number of candidate structures.^{26–31}

In brief, the search for the global minimum using a GA is performed in the 3N configurational space with the energy value as a comparison criterion. The individuals of the initial population are randomly generated, where the maximum cluster volume can be defined by the user as a function of the cluster size. More details of the algorithm used can be found in a previous publication.²⁴

The search using the GA was performed for the $n \leq 5$ (LiF)_nF[−] cluster ions, and the calculations were carried at the DFT/B3LYP/3-21G level of theory using the Gaussian 03 software.³² As in the previous work,²⁴ the population size was chosen to be from 15 to 20 individuals, and the GA was terminated after 50 generations, which is good enough to find the global minimum and low-energy isomers. The energy convergence criteria was set to 10^{-5} hartree.³²

3.2. Optimization of the Candidate Structures. Theoretical calculations have been performed at the DFT/B3LYP/6-311+G(3df), DFT/B3LYP/LACV3P*+, and MP2/LACV3P*+ levels with the purpose of determining the geometrical parameters, internal energies, and charge distributions of the most stable structures of the (LiF)_nF[−] and (LiF)_n[−] series. In the case of the (LiF)_n[−] series, only the linear structures were considered. These new results complement the previous reported results for the (LiF)_nLi⁺, (LiF)_nLi⁰, and (LiF)_n⁰ cluster structures.²⁴ The “pool” of candidate structures (for $n \leq 5$), generated using the GA algorithm, has been used as initial geometries for the optimization process. The larger clusters ($n > 5$) were mainly analyzed with the Jaguar 6.0 software³³ using the pseudospectral method to minimize the computational time. No symmetry restrictions have been imposed in the process of geometry optimization. A vibration frequency analysis was performed for all optimized structures at the level of calculation employed. For the reported structures, all frequencies are observed to be real, indicating that they correspond to the true minima in the respective potential energy hypersurfaces.

It is well known that DFT calculations on charged species may be in error because of the fact that for most of the present available functionals the exchange energy does not exactly cancel the Coulombic self-interaction.³⁴ This effect becomes less important as the number of atoms increases. It is also important to mention that DFT calculations may not properly describe the systems that are dominated by dispersion forces.³⁵ To check for possible inconsistencies, the smaller structures ($n < 6$) were also optimized at the MP2/LAVCV3P* level of calculation. No substantial changes were observed either in the geometrical parameters or in the relative stability of the clusters. We investigated the nature of the charge distribution on the LiF clusters by computing the atomic charges using the CHelpG

algorithm.³⁶ The energy values of the optimized structures were corrected for the zero-point energy (ZPE) to obtain the total energy E_T ($E_T = \text{SCF} + \text{ZPE}$), a crucial quantity for the analysis of the isomers stability.

3.3. D-Plot Methodology. Details of the D-plot methodology can be found elsewhere.^{24,37–39} In brief, the D-plot is a practical method for displaying the relative stability of the clusters by representing the total energy (E_T) of a given cluster of size n and charge q as a function of the average energy of all of the n isomers, $\langle E(n, q) \rangle$, plus a certain energy deviation, $D(n, q, i)$. Because, in general, the average energy $\langle E(n, q) \rangle$ increases linearly with the cluster size n of the form (XY)_nX⁺ or (XY)_nY[−], the total energy $E_T(n)$ can be expressed as

$$E_T(n) = \langle E(n, q) \rangle + D(n, q, i) = E_0 - nE_{XY} + D(n, q, i) \quad (1)$$

where E_0 is the total energy of the X⁺ or Y[−] atomic ions and the slope coefficient, E_{XY} , is the average total energy of the neutral XY molecule. Because $D(n, q, i) \ll (E_0 - nE_{XY})$, these two parameters are rather insensitive to the number of configurations employed, which is not the case for $D(n, q, i)$. Lower $D(n, q, i)$ values correspond to lower-energy isomers and thus more stable structures. In practice, E_0 and E_{XY} are parameters determined from the linear fit over all predicted configurations. The relevant features of the D-plot are (i) the most stable isomers are promptly determined and (ii) the cluster families can be easily identified according to their trends in the D-plot^{24,37–39} as long as enough members of the series are obtained to allow unambiguously continuous curves to be drawn that connect the D-values of the members of the series.

4. Results and Discussion

4.1. Experimental Results. A typical negative ion PDMS-TOF spectrum of a ⁷LiF polycrystalline target is presented in Figure 1. The mass resolution of the spectrometer was sufficient to allow unambiguous peak assignments. In the mass <100 u region (Figure 1a), the desorption yields of the $n = 0$ to 3 members of the (LiF)_nF[−] series are comparable to those of other molecules absorbed in the ⁷LiF surface (e.g., pump oil contaminants), whereas in the 100–600 u mass region (Figure 1b), the (LiF)_nF[−] cluster ions are dominant and easily identified. Note that the peak corresponding to the mass 149 u is the highest in Figure 1b, indicating high stability of the “magic number” $n = 5$ configuration. This abrupt change of desorption yield behavior at $n = 5$ suggests a change of the dominant production mechanism, the relative cluster stability, or both.

4.1.1. F[−] Emission. The F[−] ion emission is distinct from that of other SIs. For example, (i) close inspection of Figure 1a reveals that the F[−] desorption yield (i.e., the counts corresponding to each peak divided by the number of projectiles) is remarkably low compared with the other low mass SIs; (ii) such relative low yield is similar to that observed for I[−] SIs when CsI is bombarded by 333 MeV ²³⁸U,¹⁴ (iii) because the angular distribution of I[−] ions is roughly isotropic whereas that of Cs⁺ ions goes¹⁴ as $\cos^3 \theta$, it is expected that the same situation occurs for the F[−] and Li⁺ emission; (iv) the F[−] desorption yield decreases with the projectile velocity, whereas the Li⁺ and (LiF)Li⁺ desorption yields increase;¹⁶ (v) the axial initial velocity distribution of F[−] ions is larger than that of C₂H[−] secondary ions, which are produced by purely electronic sputtering;^{15,40} and (vi) the shapes of the axial initial velocity distributions of F[−] ions produced by the impact of N₂ or N beams are the same and agree with the linear cascade theory prediction.⁴⁰

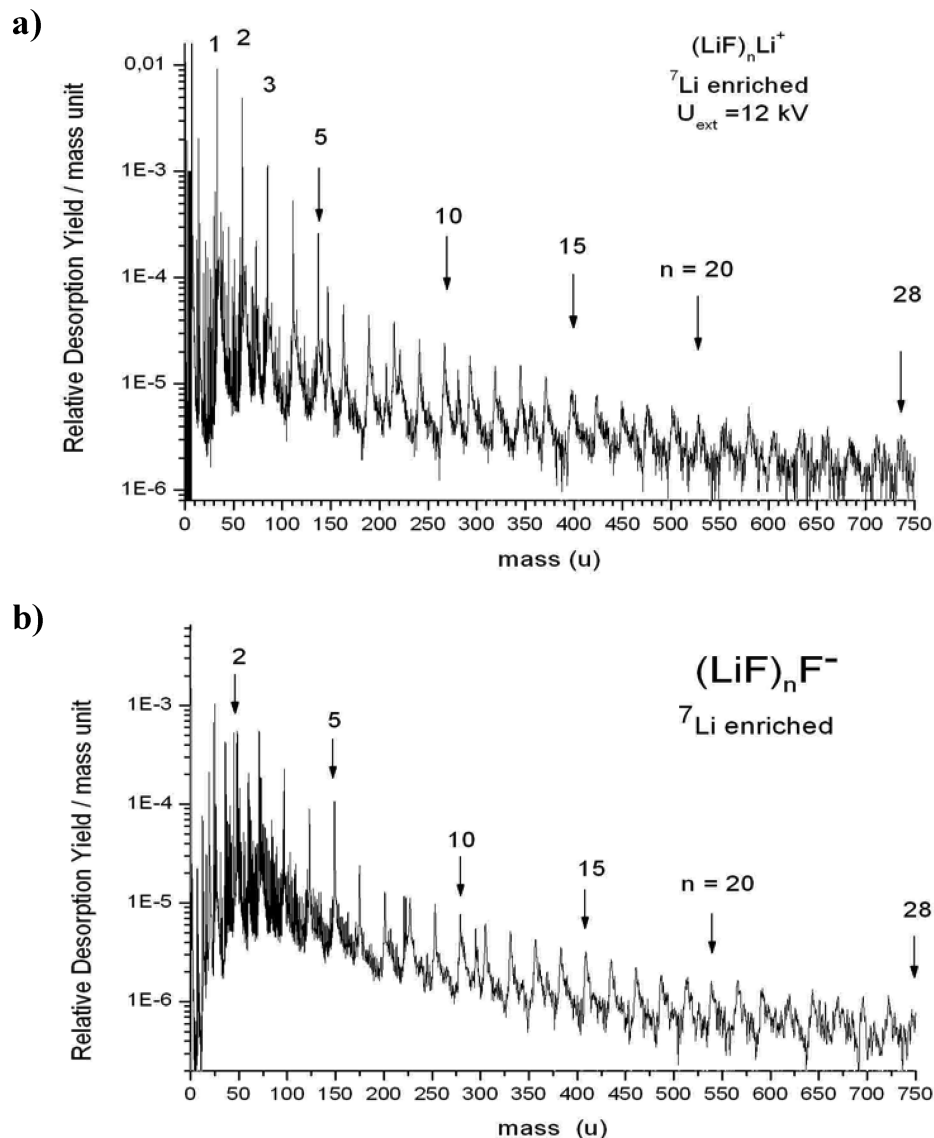


Figure 2. Comparison between ^7LiF mass spectra of (a) positive and (b) negative secondary cluster ions. Their shapes are similar but the relative desorption yields of positive ions are higher. Note the sharp yield decrease for both spectra after the $n = 5$ cluster peak.

These findings support the hypothesis that most of the target F^- species interacting with the projectile loose an electron and become neutral. The secondary electron emission locally destabilizes the positively charged LiF region causing the emission of F^0 and Li^+ species via an electronic regime and, as a consequence, their desorption yield should follow the electronic stopping power dependence on the projectile velocity. On the contrary, the emission of F^- ions is due to a collision cascade inside the target, and the F^- ions desorption yield follows the nuclear stopping power. Therefore, there are two main reasons for the relatively low yield of the F^- ions: the nuclear stopping power is much lower than the electronic stopping power for MeV/u projectiles, and F^- ions excited over 3.4 eV are neutralized by electron detachment.^{41,42}

4.1.2. $(\text{LiF})_n^-$ Series. The emission of LiF^0 species by ion beam impact is expected to be a main process of LiF sputtering. During desorption, electron detachment or capture by the neutral species can lead to the production of $(\text{LiF})_n^+$ or $(\text{LiF})_n^-$ cluster ions. The desorption yield of the $(\text{LiF})_n^+$ series has been reported to be more than one order of magnitude lower than that of the $(\text{LiF})_n\text{Li}^+$ series,²⁴ and the same result is observed for the negative series. The ratio between the F^- yield and the 26 u peak (sum of the LiF^- and C_2H_2^- contributions) yield is 3.2.

The 52 u species yield, $(\text{LiF})_2^-$ is 2.9 times lower than that of the 26 u species. No peak is observed at the mass corresponding to the $(\text{LiF})_3^-$ member.

4.1.3. $(\text{LiF})_n\text{F}^-$ Series. The $(^7\text{LiF})_n^7\text{Li}^+$ and the $(^7\text{LiF})_n\text{F}^-$ cluster ion series are the most abundant SIs observed during the ^7LiF bombardment. Figure 2 shows the comparison of both spectra. The background is very low, and its shape is determined by the overlap of long peak tails produced by delayed cluster ions formed in the acceleration region of the spectrometer.

The desorption yields of the $(^7\text{LiF})_n^7\text{Li}^+$ and $(^7\text{LiF})_n\text{F}^-$ cluster ions are displayed in Figure 3 as a function of n . The yield distributions over the total mass range may be divided into three regions: (i) the light mass region ($n = 0$ and 1), where both distributions have opposite behavior (of the derivative), (ii) the medium mass range ($2 \leq n \leq 5$), where they have the same behavior and a steep slope, and (iii) the heavy mass region ($n \geq 6$), where both yields show the same monotonical slow decrease. Except in the light mass region, the negative cluster ion yields are almost a factor of four lower than those of the corresponding $(^7\text{LiF})_n^7\text{Li}^+$ series members. Such unbalanced desorption yield is attributed to the secondary electron emission because the free electrons originate mainly from the anion species precursors.

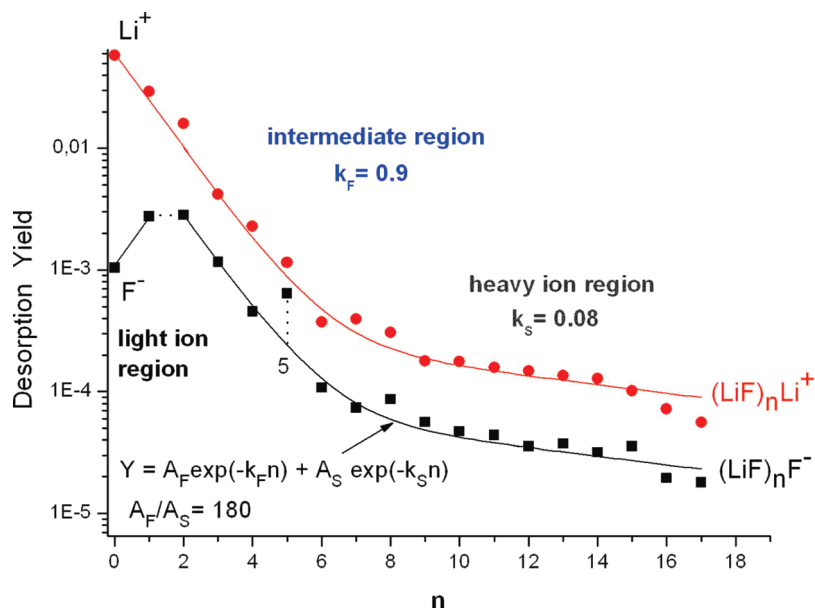


Figure 3. Desorption yield distribution of $(\text{LiF})_n\text{Li}^+$ (●) and $(\text{LiF})_n\text{F}^-$ (■) cluster ions. On the basis of the slope of the distribution, $n = 2$ and 5 define three regions: for $n = 1$ and 2, the yield of positive ions are one order of magnitude higher; for $n \geq 2$, the distributions are proportional to each other (by a factor of ~ 4). The solid lines are fittings using the indicated expression. The yield of the “magic number” $n = 5$ at the border of two regions deviates strongly from the fitting.

A surprising result is the fact that both yield distributions can be fitted by the sum of two decreasing exponential functions, $Y = A_F \exp(-k_F n) + A_S \exp(-k_S n)$, whose fast and slow decay parameters are the same for negative and positive cluster ions: $k_F = 0.9$ and $k_S = 0.08$, respectively. Moreover, such behavior has been reported only for megaelectronvolt bombardment of condensed gas targets that have about the same values⁴³ for k_F and k_S . The origin of the fast and slow yield decrease (characterizing the medium and heavy mass regions) remains unclear but is a signature of an important and general behavior related to electronic sputtering processes. It has been suggested that the medium mass range (clusters having $2 \leq n \leq 5$) is best described by cluster synthesis (recondensation in the gas phase, just after the local crystal dissociation into atomic and molecular species by each projectile), whereas the light mass region is due to unattached or detached light species, and the heavy mass region ($n \geq 6$) corresponds to large and cold preformed crystal debris emission.⁴³ Accordingly, the formation of the medium-sized clusters is ruled by the stability of the cluster structure in contrast with the large clusters whose structures reflect that of the target crystal.

4.1.4. $(\text{LiF})_n^0$ Emission. As mentioned before, the $(\text{LiF})_n^0$ secondary emission is expected to exhibit the highest desorption yield. Although the yield and the shape of the neutral cluster distribution cannot be directly determined by mass spectrometry, the fact that the positive and negative secondary cluster ions show the same yield distribution (Figures 2 and 3) strongly suggests that the neutral cluster distribution should present the same shape. On the basis of this assumption, preliminary sputtering mechanism may be considered for the neutral secondary emission analysis, as will be further discussed.

4.2. Theoretical Results. The structure and internal energies of positive and neutral LiF clusters have been previously reported.²⁴ Repeating the same procedure, the GA algorithm (for $n \leq 5$) was used to generate the structures for the most abundant $(\text{LiF})_n\text{F}^-$ series observed in the experiments. A total of 46 structures was found for the $(\text{LiF})_n\text{F}^-$ series, with $n = 1$ to 9. The structures were labeled according to the same notation as that used for the positive and neutral LiF clusters.²⁴ That is,

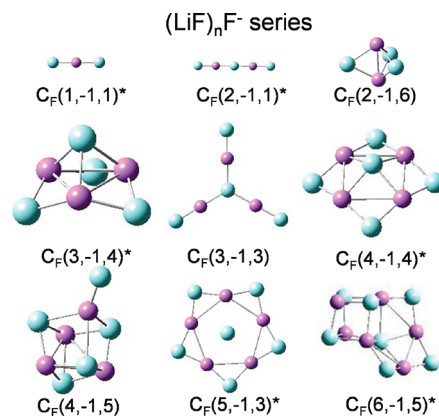


Figure 4. Some members of the $(\text{LiF})_n\text{F}^-$ series, $C_F(n, -1, i)$. Lowest-energy isomers are denoted by *. All optimized structures are available in the Supporting Information.

each isomer structure is labeled as $C(n, q, i)$, where n is the cluster size, q is the charge, and i is the isomer index that characterizes the family type, total energy, or both: $i = 1$ for the linear isomers, $i = 2$ for the planar rhombus family, and $i = 3$ for regular polygons or cyclic planar shapes. Values of $i \geq 4$ denote 3D structures: $i = 4$ for cyclic parallel polygons or pyramidal shapes, $i = 5$ for cubic or cubelike structures (tending to a fcc one), and $i > 5$ for others 3D shapes (chair, spherical-like, etc.).

Figure 4 shows some of the DFT structures found for the $(\text{LiF})_n\text{F}^-$ series and classified according to the $C_F(n, -1, i)$ notation. The total energy (E_T), the deviation relative to the isomeric linear structure (ΔLin), and the total deviation energy ($D(n, -1, i)$) values are given in Table 1. For $n = 1$, only the linear structure $\text{F}-\text{Li}-\text{F}^-$ was found to be stable. The 2D structures grow from either a kitelike structure toward more complex kite- and rhombiclike structures or from a starlike structure. The 3D configurations are basically cubelike, pyramidal, and polyhedral-like. In the case of the $(\text{LiF})_n^-$ series, only the linear isomers were considered, and following the same notation, this series can be denoted as $C(n, -1, 1)$. The total

TABLE 1: Theoretical Results for the $(\text{LiF})_n\text{F}^-$ Cluster Series

$C_F(n, -1, i)$			DFT/B3LYP/6-311+G(3df)			
n	i	type of structure	SCF+ZPE [hartree]	E_T [eV]	ΔLin (eV)	D_n (eV)
0		atomic F-	-99.8886932	-2718.13		0.74
1	1	linear	-207.470323	-5645.60		-0.15
2	1	linear	-315.021411	-8572.24		-0.21
2	2	kite	-315.004955	-8571.79	0.45	0.24
2	6	diamond	-314.994748	-8571.51	0.73	0.52
3	4	pyramid	-422.576126	-11 498.97	-0.28	-0.36
3	1	linear	-422.565739	-11 498.69		-0.08
3	2	kite	-422.560808	-11 498.56	0.13	0.05
3	2	rhombus grid	-422.557149	-11 498.46	0.23	0.15
3	7	kite-diamond	-422.549052	-11 498.24	0.45	0.37
3	3a	star	-422.540097	-11 497.99	0.70	0.62
3	6	diamond	-422.530358	-11 497.73	0.96	0.88
4	4	pyramid	-530.148160	-14 426.18	-1.11	-0.99
4	7	kite-rhombus	-530.128213	-14 425.64	-0.57	-0.45
4	7	kite-rhombus	-530.116100	-14 425.31	-0.24	-0.12
4	7	kite-rhombus	-530.114973	-14 425.28	-0.20	-0.09
4	7	kite-rhombus	-530.113500	-14 425.24	-0.16	-0.05
4	5	cubelike	-530.112855	-14 425.22	-0.15	-0.03
4	4	rhombuslike	-530.111754	-14 425.19	-0.12	0.00
4	7	kite-pyramid	-530.109168	-14 425.12	-0.05	0.07
4	1	linear	-530.107444	-14 425.07		0.12
4	2	rhombus grid	-530.106252	-14 425.04	0.03	0.15
4	7	kite-pyramid	-530.096268	-14 424.77	0.30	0.42
4	2	rhombus grid	-530.093002	-14 424.68	0.39	0.51
4	3	starlike	-530.086193	-14 424.49	0.58	0.70
4	4	rhombuslike	-530.082332	-14 424.39	0.68	0.80
5	3	starlike	-637.703005	-17 352.92	-1.50	-1.15
5	3	starlike	-637.702522	-17 352.91	-1.49	-1.14
5	4	rhombuslike	-637.689894	-17 352.56	-1.14	-0.79
5	4	rhombuslike	-637.686801	-17 352.48	-1.06	-0.71
5	5	cubelike	-637.686789	-17 352.48	-1.06	-0.71
5	7	kite-rhombus	-637.686729	-17 352.48	-1.06	-0.71
5	2	rhombus grid	-637.681344	-17 352.33	-0.91	-0.56
5	4	pyramid-like	-637.673634	-17 352.12	-0.70	-0.35
5	5	cubelike	-637.670310	-17 352.03	-0.61	-0.26
5	5	cubelike	-637.668581	-17 351.98	-0.56	-0.21
5	4	rhombus like	-637.666413	-17 351.92	-0.50	-0.15
5	5	cubelike	-637.665640	-17 351.90	-0.48	-0.13
5	2	rhombus grid	-637.655340	-17 351.62	-0.20	0.15
5	5	cubelike	-637.653673	-17 351.58	-0.16	0.19
5	1	linear	-637.647907	-17 351.42		0.35
6	5	cubelike	-745.251279	-20 279.48	-1.73	-1.13
6	4	pyramidlike	-745.244280	-20 279.29	-1.54	-0.94
6	1	linear	-745.187677	-20 277.75		0.60
7	1	linear	-852.726546	-23 204.05		0.88
8	1	linear	-960.266469	-26 130.39		1.12
9	1	linear	-1067.80549	-29 056.70		1.39

energy (E_T), and total deviation energy ($D(n, -1, 1)$) values for the $(\text{LiF})_n^-$ and $(\text{LiF})_n^0$ linear isomers are given in Table 2. All optimized geometries are supplied as Supporting Information.

Figure 5 shows the total deviation energies $D(n, -1, i)$ as a function of the cluster size n for the members of the $(\text{LiF})_n\text{F}^-$ series (top) and for the linear structures of the $(\text{LiF})_n^-$ series (bottom). Note that the fact that the D values are in the electronvolt range whereas the total energies are in the kiloelectronvolt range (Tables 1 and 2) allows a better visualization of the relative isomer's stability as function of the cluster size n . The lower the D value, the higher the relative stability of the isomer. Inspection of Figure 5 (top) shows that a transition in stability from linear to 2D and 3D structures occurs at $n \approx 3$. That is, for the linear structures $C_F(n, -1, 1)$, the function D is negative up to $n = 3$, after which it becomes positive and starts to increase linearly with n . This trend suggests that the lower cluster sizes ($n = 1$ to 3) present the highest stability. Figure 5 (bottom) shows that for the $(\text{LiF})_n^-$ linear series the function D

is negative for $n = 3$ to 5; that is, the highest stability is predicted for the medium-sized clusters. For the $(\text{LiF})_n\text{F}^-$ series, as the cluster size increases, a larger variety of isomers is also observed. Not all expected structures are observed, a result that reflects the fact that the $(\text{LiF})_n\text{F}^-$ cluster ions are stabilized not only by short-range interactions but also by the average interaction of all cluster counterparts, as will be further discussed. These findings are similar to those previously reported for the $(\text{LiF})_n\text{Li}^+$, $(\text{LiF})_n\text{Li}^0$, and $(\text{LiF})_n^0$ series and may be a consequence of the ionic bonding nature of the LiF clusters.

An attempt to understand the relative stabilities of the clusters can be made on the basis of their structures and charge distributions. Atomic charges, obtained from the ChelpG algorithm, as well as the clusters' optimized geometries are included in the Supporting Information. The inspection of the optimized structures shows a certain degree of symmetry, which could be related to the ionic bonding nature of the LiF clusters. The symmetry in the relative position of the atoms in the cluster is also observed in their atomic charge values. In the case of

TABLE 2: Theoretical Results for the $(\text{LiF})_n^-$, $(\text{LiF})_n^0$, and $(\text{LiF})_n\text{F}^0$ Linear Series

$(\text{LiF})_n^-$ linear series					
$C(n, -1, i)$			DFT/B3LYP/6-311+G(3df)		
n	i	type of structure	SCF+ZPE [hartree]	E_T [eV]	D_n (eV)
1	1	linear	-107.487765	-2924.91	0.08
2	1	linear	-215.032035	-5851.37	0.00
3	1	linear	-322.575648	-8777.80	-0.05
4	1	linear	-430.117428	-11 704.18	-0.05
5	1	linear	-537.658033	-14 630.54	-0.03
6	1	linear	-645.197902	-17 556.87	0.02
7	1	linear	-752.737183	-20 483.18	0.09

$(\text{LiF})_n^0$ linear series					
$C(n, 0, i)$			DFT/B3LYP/6-311+G(3df)		
n	i	type of structure	SCF+ZPE [hartree]	E_T [eV]	D_n (eV)
		atomic F neutral	-99.761681	-2714.67	
1	1	linear	-107.46949	-2924.42	-0.29
2	1	linear	-214.988136	-5850.17	0.11
3	1	linear	-322.518622	-8776.25	0.18
4	1	linear	-430.053196	-11 702.44	0.14
5	1	linear	-537.589333	-14 628.67	0.06
6	1	linear	-645.126269	-17 554.92	-0.04
7	1	linear	-752.663501	-20 481.18	-0.15

$(\text{LiF})_n\text{F}^0$ linear series					
$C_F(n, 0, i)$			DFT/B3LYP/6-311+G(3df)		
n	i	type of structure	SCF+ZPE [hartree]	E_T [eV]	D_n (eV)
0		atomic F neutral	-99.761681	-2714.67	
1	1	linear	-207.269318	-5640.13	0.06
2	1	linear	-314.803156	-8566.30	0.06
3	1	linear	-422.340514	-11 492.56	-0.03
4	1	linear	-529.878531	-14 418.84	-0.14
5	1	linear	-637.416692	-17 345.13	-0.26
6	1	linear	-744.954889	-20 271.41	-0.37

2D and 3D structures, multipole interactions are mainly responsible for the total cluster stability. The effects of the symmetry and of the relative importance of monopole–dipole

and dipole–dipole interactions for the cluster stability can be analyzed in the simpler scenario provided by the 1D structures. The analysis closely follows the one presented for the positive clusters.²⁴ The atomic charge distribution of the $(\text{LiF})_n\text{F}^-$ linear clusters is symmetric relative to the central part of the structure and decreases in absolute value, from the central part to both ends of the linear chain. These clusters can be described as being constituted by LiF units symmetrically displaced relative to the central part of the structure (Li for n odd or Li–F–Li for n even). For n even, the dipole moment of the central (Li–F–Li) unit vanishes by symmetry. The atomic charges on the LiF units do not dramatically change with the cluster size, and the total value is a function of their position relative to the central part of the linear structure. Therefore, because of this particular atomic charge distribution, the cluster is stabilized by dipole–dipole interactions between the LiF units and dipole–monopole interaction between the LiF units and the center part of the structure (Li for n -odd or Li–F–Li for n -even). As the cluster size increases, weaker interactions are expected because of the larger distances from the LiF units to the central part of the linear structure. This is evidenced in Figure 5 (top) by the trend in the D values: the interactions are strong for $n = 2$ and 3 and become weaker as the cluster size increases.

For the $(\text{LiF})_n^-$ series, the atomic charge distribution is not symmetric anymore and some charge is shifted to the ends of the linear chain. Not only do the terminal atoms (Li or F) present larger absolute charges but the terminal LiF units also exhibit a large dipole moment. The interactions between these (LiF) terminal units with the rest of the structure via dipole–dipole interactions are responsible for the structure stability. As the size increases, a maximum of stability is observed for $n = 3$ and 4. Analogous to the $(\text{LiF})_n\text{F}^-$ series, this type of interaction is distance-dependent, which is evidenced by the decrease in stability for the clusters with $n > 4$ (Figure 5, bottom).

The relative stability of the cluster structures can also be analyzed by examining the fragmentation energy as a function of the cluster size. The fragmentation energy, FE, is the difference between the cluster energy and the sum of the energies of the isolated fragments produced by the dissociation of the cluster. Theoretical values of FE, calculated from the total energies, E_T , for selected fragmentation channels, are contained in Tables 3. The dissociation process is better understood when examined for fragmentation into structures of the same cluster series. In this case, structural rearrangements can be neglected, and the main differences can be attributed to the loss of LiF units. For the linear $(\text{LiF})_n\text{F}^-$ clusters, one may consider fragmentation processes without or with charge transfer from the $(\text{LiF})_n\text{F}^-$ to the $(\text{LiF})_n^-$ linear series. The respective fragmentation energies are defined by eqs 2 and 3

$$\text{FE}_{\text{NT}}(n, m) = E_T[(\text{LiF})_m\text{F}^-] + E_T[(\text{LiF})_{n-m}^0] - E_T[(\text{LiF})_n\text{F}^-] \quad (2)$$

$$\text{FE}_T(n, m) = E_T[(\text{LiF})_m\text{F}^0] + E_T[(\text{LiF})_{n-m}^-] - E_T[(\text{LiF})_n\text{F}^-] \quad (3)$$

Theoretical values of FE, calculated from the total energies E_T for selected fragmentation channels, are shown in Table 3. The $\text{FE}_{\text{NT}}(n, n - 1)$ values are the binding energies of the precursor cluster ($n - m = 1$) for LiF⁰ emission. Figure 6 shows the fragmentation energy dependence on the cluster size for some of the channels presented in Table 3. As illustrated in

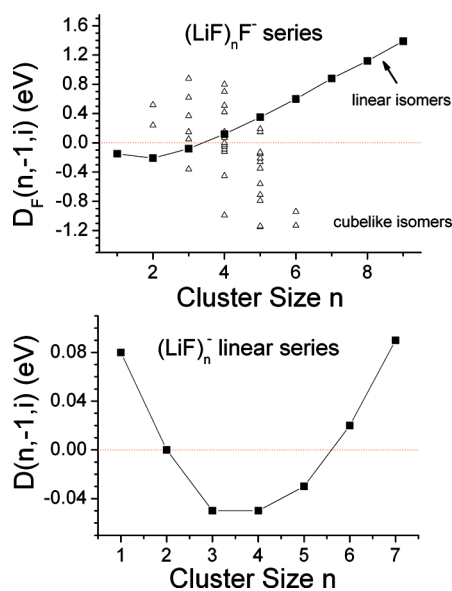


Figure 5. Total energy deviations as a function of the cluster size. Top: $D_F(n, -1, i)$ for the $(\text{LiF})_n\text{F}^-$ ions. Bottom: $D(n, -1, i)$ for the $(\text{LiF})_n^-$ linear series. The square symbols represent the linear isomers and the triangle symbols refer to the cubelike isomers.

TABLE 3: Fragmentation Energy Dependence on the Cluster Size for the $(\text{LiF})_n\text{F}^-$, $(\text{LiF})_n\text{F}^0$, and $(\text{LiF})_n^0$ Linear Series with $\text{FE}_\text{T}(n, m)$ and Without $\text{FE}_\text{NT}(n, m)$ Charge Transfer (See Text)

$(\text{LiF})_n\text{F}^- \rightarrow (\text{LiF})_m\text{F}^- + (\text{LiF})_{n-m}^0$					
$\text{FE}_\text{NT} \text{ (eV)}$					LiF^0
n	$m = 0$	$m = 1$	$m = 2$	$m = 3$	
1	3.05				3.05
2	3.93	2.22			2.22
3	4.31	2.92	2.04		2.04
4	4.51	3.22	2.66	1.97	1.97
5	4.62	3.38	2.94	2.56	1.93
6	4.70	3.48	3.08	2.81	1.91
7	4.74	3.54	3.15	2.93	1.89
8		3.61	3.23	3.03	1.92
9			3.28	3.09	1.89

$(\text{LiF})_n\text{F}^- \rightarrow (\text{LiF})_m\text{F}^0 + (\text{LiF})_{n-m}^-$					
$\text{FE}_\text{T} \text{ (eV)}$					LiF^-
n	$m = 0$	$m = 1$	$m = 2$	$m = 3$	
1	6.01				6.01
2	6.20	7.19			7.19
3	6.22	7.19	7.48		7.48
4	6.21	7.14	7.41	7.60	7.60
5	6.21	7.11	7.32	7.49	7.66
6	6.21	7.08	7.27	7.39	7.71
7	6.20	7.06	7.22	7.31	7.73
8		7.07	7.22	7.29	
9			7.22	7.27	

$(\text{LiF})_n\text{F}^0 \rightarrow (\text{LiF})_m\text{F}^0 + (\text{LiF})_{n-m}^0$					
$\text{FE}_\text{NT} \text{ (eV)}$					LiF^0
n	$m = 0$	$m = 1$	$m = 2$	$m = 3$	
1	1.04				1.04
2	1.45	1.75			1.75
3	1.64	2.26	1.85		1.85
4	1.73	2.47	2.37	1.86	1.86
5	1.79	2.56	2.58	2.40	1.87
6	1.82	2.62	2.68	2.61	1.87

$(\text{LiF})_n^0 \rightarrow (\text{LiF})_m^0 + (\text{LiF})_{n-m}^0$					
$\text{FE}_\text{NT} \text{ (eV)}$					LiF^0
n	$m = 0$	$m = 1$	$m = 2$	$m = 3$	
1					
2		1.34			1.34
3		1.66	1.66		1.66
4		1.77	2.09	1.77	1.77
5		1.81	2.25	2.25	1.81
6		1.84	2.31	2.42	1.84
7		1.84	2.34	2.49	1.84

Figure 6 (top), if no charge transfer occurs during the fragmentation of the $(\text{LiF})_n\text{F}^-$ clusters, the most and the least energetically favorable channels are the emission of a neutral LiF unit and of a F^- ion, respectively. If charge transfer from the $(\text{LiF})_n\text{F}^-$ to the $(\text{LiF})_n^-$ fragment occurs (Figure 6, bottom), then higher FE values are determined. For the FE_T process, the most energetically favorable channel is the emission of a neutral F atom, whereas the least energetically favorable channel is the emission of a negatively charged LiF^- unit. Comparison of the FE_NT and FE_T values suggests that the dissociation without charge transfer is up to 3 times more favorable among the lower energy channels. (See Figure 6.) For the $(\text{LiF})_n\text{F}^0$ series, although its members are not observed experimentally, the most energetically favorable channels are the emission of a neutral F atom, followed by the emission of a neutral LiF^0 unit.

In summary, these results indicate that (i) large $(\text{LiF})_n\text{F}^-$ linear cluster ions decay preferentially by neutral LiF^0 emission; (ii) a successive loss of LiF^0 units is more likely to occur than a single $(\text{LiF})_m^0$ cluster emission; (iii) fragmentation of $(\text{LiF})_n\text{F}^-$ linear cluster ions into F^0 , F^- , or $(\text{LiF})\text{F}^-$ is attenuated; and (iv) $(\text{LiF})_n^-$ clusters are not likely to be formed from their $(\text{LiF})_n\text{F}^-$ precursors.

Although neither the linear $(\text{LiF})_n\text{F}^0$ nor the $(\text{LiF})_n^0$ clusters can be observed directly by mass spectrometry, fragmentation energies, $\text{FE}_\text{NT}(n, m)$, can be predicted. For example, fragmentation energies for processes that involve only the production of neutral species can be computed from eqs 4 and 5

$$\text{FE}_\text{NT}(n, m) = E_\text{T}[(\text{LiF})_m\text{F}^0] + E_\text{T}[(\text{LiF})_{n-m}^0] - E_\text{T}[(\text{LiF})_n\text{F}^0] \quad (4)$$

$$\text{FE}_\text{NT}(n, m) = E_\text{T}[(\text{LiF})_m^0] + E_\text{T}[(\text{LiF})_{n-m}^0] - E_\text{T}[(\text{LiF})_n^0] \quad (5)$$

The obtained FE values are displayed in Table 3, and the fragmentation energy dependence on the cluster size is shown in Figure 7. The results suggest that the most energetically favorable channels always involve the smallest possible neutral fragment. For the $(\text{LiF})_n\text{F}^0$ series, the preferred emission is the F^0 atom, followed by the emission of a neutral LiF^0 unit. In the case of the $(\text{LiF})_n^0$ series, the smaller the $(\text{LiF})^0$ unit, the smaller the FE value.

From the E_T values presented in Tables 1 and 2, electron affinities (EAs) can be determined for the neutral LiF clusters. (See Table 4.) Of course, these values are equal, in modulus, to the first ionization potential (or detachment energy) of the respective negative ions. Experimental values of electron affinity for molecules and clusters are scarce, but for $n = 0$, the EA of $(\text{LiF})_n\text{F}$ is just, of course, the fluorine EA. Blondel et al.,⁴⁴ using the laser photodetachment technique, obtained a value of 3.401 eV for the EA of fluorine, which is in excellent agreement with

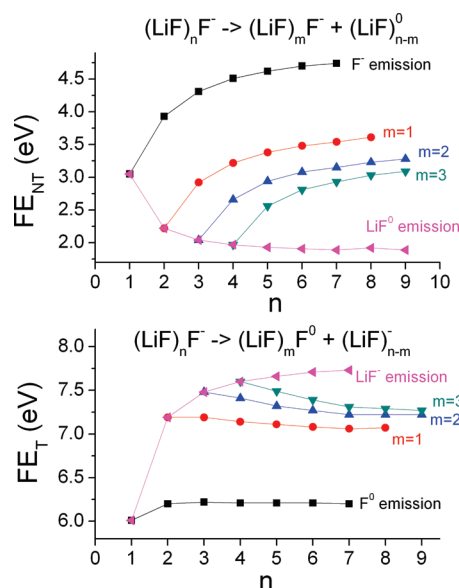


Figure 6. Fragmentation energy dependence on the cluster size for the linear $(\text{LiF})_n\text{F}^-$ series. Top: fragmentation without charge transfer for the $(\text{LiF})_n\text{F}^-$ linear series $\text{FE}_\text{NT}(n, m)$. Bottom: fragmentation with charge transfer from the $(\text{LiF})_n\text{F}^-$ to the $(\text{LiF})_n^-$ linear series $\text{FE}_\text{T}(n, m)$.

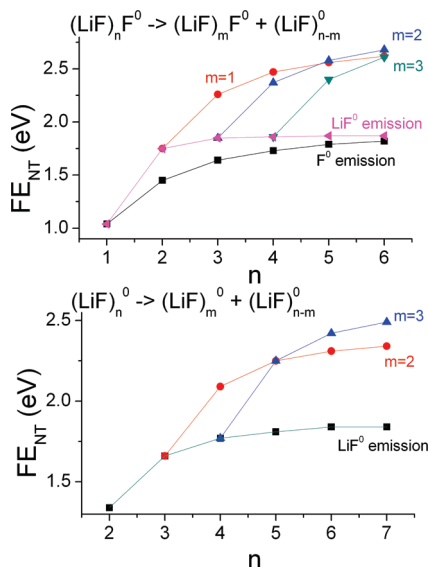


Figure 7. Fragmentation energy dependence on the cluster size for the linear $(\text{LiF})_n\text{F}^0$ and $(\text{LiF})_n^0$ series. Top: fragmentation without charge transfer for the $(\text{LiF})_n\text{F}^0$ linear series $\text{FE}_{\text{NT}}(n, m)$. Bottom: fragmentation without charge transfer for the $(\text{LiF})_n^0$ linear series $\text{FE}_{\text{NT}}(n, m)$.

TABLE 4: Electron Affinity Dependence on the Cluster Size for the $(\text{LiF})_n\text{F}$ and $(\text{LiF})_n$ Linear Species

n	electron affinity (eV)	
	$(\text{LiF})_n\text{F}$	$(\text{LiF})_n$
0	3.46	
1	5.47	0.50
2	5.94	1.19
3	6.13	1.55
4	6.23	1.75
5	6.29	1.87
6	6.33	1.95

the value (3.46 eV) reported in Table 4. Therefore, we believe that the EA values for the other species listed in the table should be equally reliable.

The dependence of the electron affinity values on the cluster size is illustrated in Figure 8 for linear structures, and general trends can be summarized: (i) the members of the $(\text{LiF})_n$ series present lower electron affinities than those calculated for the $(\text{LiF})_n\text{F}$ series and (ii) the electron affinity of both $(\text{LiF})_n\text{F}$ and $(\text{LiF})_n$ species increases monotonically with n but levels off around $n \approx 5$. These results suggest that the neutralization of the $(\text{LiF})_n^-$ ion clusters is much more likely to occur than the

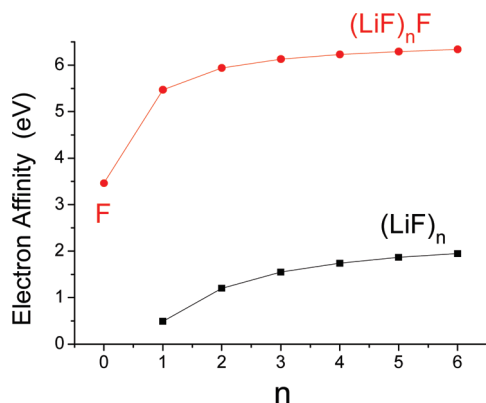


Figure 8. Electron affinity dependence on the cluster size for the $(\text{LiF})_n\text{F}$ and $(\text{LiF})_n$ species.

neutralization of the $(\text{LiF})_n\text{F}^-$ ions and provide an explanation for the fact that the observed desorption yield of the $(\text{LiF})_n^-$ ions is lower than that of the $(\text{LiF})_n\text{F}^-$ ions. The electron affinity increases with n because electronic delocalization also increases with the size of the clusters. Such an increase levels off when the delocalization saturates, that is, when the interaction between the two ends of the linear cluster becomes negligible. For the $(\text{LiF})_n\text{F}^-$ series, the electron affinity values are lower than the fragmentation energy thresholds for $(\text{LiF})_m^-$ emission but higher than the fragmentation energy thresholds for $(\text{LiF})_m\text{F}^-$ (especially for large clusters). This is in good agreement with the experimental relative abundances observed for the $(\text{LiF})_m\text{F}^-$ series as a function of the cluster size. Note also in Figure 8 that the electron affinity increases by a factor of ~ 2 as n varies from 0 to 4. Therefore, the process of electron detachment will be more effective for neutralizing the smaller cluster anions formed, thus contributing to a reduction of their desorption yields.

5. Conclusions

The secondary ion emission of negative ions from a polycrystalline ^7LiF target under MeV bombardment is essentially constituted of $(^7\text{LiF})_n\text{F}^-$ cluster ions, although their desorption yield distributions are much lower than those for the positive $(^7\text{LiF})_n\text{Li}^+$ series previously reported.

The $(^7\text{LiF})_n\text{F}^-$ distribution presents a maximum at $n = 2$ or 3. The lower desorption yields of the negative ions may be attributed to an abundant secondary electron emission. DFT and MP2 calculations suggest that the existence of a maximum in the $(\text{LiF})_n\text{F}^-$ yield distribution is a consequence of the fact that whereas the smaller $(\text{LiF})_n\text{F}^-$ clusters present a higher probability of losing an electron (lower IP), that is, of becoming a neutral cluster, the larger clusters have a lower probability of being formed. As the cluster size increases, the structure of the most stable members of the $(\text{LiF})_n\text{F}^-$ series changes from linear ($n < 3$) to more cubelike isomers, whereas the large clusters ($n > 6$) may be considered to be debris of the cubic-centered polycrystalline target.

The very low desorption yields observed for the $(\text{LiF})_n^-$ series are also in good agreement with the DFT and MP2 predictions because the calculations show that (i) the $(\text{LiF})_n^-$ ions have relatively low ionization potentials and (ii) the members of most abundant $(\text{LiF})_n\text{F}^-$ series decay preferentially into smaller members of the same series (by LiF^0 evaporation) rather than producing $(\text{LiF})_n^-$ species (by F^0 evaporation).

The neutral species F^0 and $(\text{LiF})^0$ are predicted to be particularly abundant as secondary particles, and despite of the fact that the $(\text{LiF})_n^0$ species cannot be directly analyzed by mass spectrometry, it is proposed that their yield distribution is proportional to that describing the $n > 2$ distribution of positive and negative cluster ions.

Acknowledgment. We acknowledge the Brazilian Agencies CNPq and Faperj for partial support.

Supporting Information Available: Optimized geometry and atomic charge distribution of the members of the $(\text{LiF})_n\text{F}^-$, $(\text{LiF})_n^-$, and $(\text{LiF})_n\text{F}^0$ series. This material is available free of charge via the Internet at <http://pubs.acs.org>.

References and Notes

- (1) Sant'Anna, M. M.; Zappa, F.; Santos, A. C. F.; de Barros, A. F. L.; Wolff, W.; Coelho, L. F. S.; de Castro Faria, N. V. *Plasma Phys. Controlled Fusion* **2004**, *46*, 1009.

- (2) Belykh, S. F.; Palitsin, V. V.; Veryovkin, I. V.; Kovarsky, A. P. *Rev. Sci. Instrum.* **2007**, *78*, 085101.
- (3) Saitoh, Y.; Mizuhashi, K.; Tajima, S. *Nucl. Instrum. Methods Phys. Res., Sect. A* **2000**, *452*, 61.
- (4) Richards, J.; Kelly, J. C. *Radiat. Eff. Defects Solids* **1973**, *19*, 185.
- (5) Taylor, J. A.; Rabalais, J. W. *Surf. Sci.* **1978**, *74*, 229.
- (6) Wittmaack, K. *Surf. Sci.* **1979**, *89*, 668.
- (7) Schweikert, E. A.; Blain, M. G.; Park, M. A.; da Silveira, E. F. *Nucl. Instrum. Methods Phys. Res., Sect. B* **1990**, *50*, 307.
- (8) Michiels, E.; Gijbels, R. *Microchim. Acta* **1983**, *81*, 277.
- (9) Main, D. E.; Standing, K. G. *Surf. Sci.* **1985**, *160*, 571.
- (10) Twu, Y. J.; Conover, C. W. S.; Yang, Y. A.; Bloomfield, L. A. *Phys. Rev. B* **1990**, *42*, 5306.
- (11) Kaercher, R. G.; da Silveira, E. F.; Barros Leite, C. V.; Schweikert, E. A. *Nucl. Instrum. Methods Phys. Res., Sect. B* **1994**, *94*, 207.
- (12) Kaercher, R. G.; da Silveira, E. F.; Blankenship, J. F.; Schweikert, E. A. *Nucl. Instrum. Methods Phys. Res., Sect. B* **1995**, *100*, 383.
- (13) Li, X.; Beck, R. D.; Whetten, R. L. *Phys. Rev. Lett.* **1992**, *68*, 3420.
- (14) Betz, G.; Wien, K. *Int. J. Mass Spectrom. Ion Processes* **1994**, *140*, 1.
- (15) Pereira, J. A. M.; de Castro, C. S. C.; Jeronimo, J. M. F.; Ponciano, C. R.; da Silveira, E. F.; Wien, K. *Nucl. Instrum. Methods Phys. Res., Sect. B* **1997**, *129*, 21.
- (16) Pereira, J. A. M.; da Silveira, E. F.; Wien, K. *Radiat. Eff. Defects Solids* **1997**, *142*, 247.
- (17) Pereira, J. A. M.; da Silveira, E. F. *Surf. Sci.* **1997**, *390*, 158.
- (18) Toulemonde, M.; Assmann, W.; Trautmann, C.; Grüner, F. *Phys. Rev. Lett.* **2002**, *88*, 057602.
- (19) Toulemonde, M.; Assmann, W.; Trautmann, C.; Grüner, F.; Mieskes, H. D.; Kucal, H.; Wang, Z. G. *Nucl. Instrum. Methods Phys. Res., Sect. B* **2003**, *212*, 346.
- (20) Lenoir, J.; Boduch, P.; Rothard, H.; Ban-d'Etat, B.; Been, T.; Cassimi, A.; Jallowy, T.; Lebius, H.; Manil, B.; Ramillon, J. M. *Nucl. Instrum. Methods Phys. Res., Sect. B* **2007**, *258*, 178.
- (21) Ponciano, C. R.; Avalos, F. E.; Rentería, A.; da Silveira, E. F. *Int. J. Mass Spectrom.* **2001**, *209*, 197.
- (22) Ponciano, C. R.; Martinez, R.; da Silveira, E. F. *J. Mass Spectrom.* **2007**, *42*, 1300.
- (23) Moria, K.; Hiraoka, K. *Int. J. Mass Spectrom.* **2008**, *269*, 95.
- (24) Fernandez-Lima, F. A.; Vilela Neto, O. P.; Pimentel, A. S.; Ponciano, C. R.; Nascimento, M. A. C.; da Silveira, E. F. *J. Phys. Chem. A* **2009**, *113*, 1813.
- (25) Michalewicz, Z. *Genetic Algorithms + Data Structures = Evolution Programs*, 3rd rev. and extended ed.; Springer-Verlag: New York, 1996.
- (26) Hartke, B. *J. Phys. Chem.* **1993**, *97*, 9973.
- (27) Xiao, Y.; Williams, D. E. *Chem. Phys. Lett.* **1993**, *215*, 17.
- (28) Zeiri, Y. *Phys. Rev. E* **1995**, *51*, 2769.
- (29) Deaven, D. M.; Ho, K. M. *Phys. Rev. Lett.* **1995**, *75*, 288.
- (30) Alexandrova, A. N.; Boldyrev, A. I. *J. Chem. Theory Comput.* **2005**, *1*, 566.
- (31) Alexandrova, A. N.; Boldyrev, A. I.; Fu, Y. J.; Yang, X.; Wang, X. B.; Wang, L. S. *J. Chem. Phys.* **2004**, *121*, 5709.
- (32) Frisch, M. J.; Trucks, G. W.; Schlegel, H. B.; Scuseria, G. E.; Robb, M. A.; Cheeseman, J. R.; Montgomery, J. A., Jr.; Vreven, T.; Kudin, K. N.; Burant, J. C.; Millam, J. M.; Iyengar, S. S.; Tomasi, J.; Barone, V.; Mennucci, B.; Cossi, M.; Scalmani, G.; Rega, N.; Petersson, G. A.; Nakatsuji, H.; Hada, M.; Ehara, M.; Toyota, K.; Fukuda, R.; Hasegawa, J.; Ishida, M.; Nakajima, T.; Honda, Y.; Kitao, O.; Nakai, H.; Klene, M.; Li, X.; Knox, J. E.; Hratchian, H. P.; Cross, J. B.; Bakken, V.; Adamo, C.; Jaramillo, J.; Gomperts, R.; Stratmann, R. E.; Yazyev, O.; Austin, A. J.; Cammi, R.; Pomelli, C.; Ochterski, J. W.; Ayala, P. Y.; Morokuma, K.; Voth, G. A.; Salvador, P.; Dannenberg, J. J.; Zakrzewski, V. G.; Dapprich, S.; Daniels, A. D.; Strain, M. C.; Farkas, O.; Malick, D. K.; Rabuck, A. D.; Raghavachari, K.; Foresman, J. B.; Ortiz, J. V.; Cui, Q.; Baboul, A. G.; Clifford, S.; Cioslowski, J.; Stefanov, B. B.; Liu, G.; Liashenko, A.; Piskorz, P.; Komaromi, I.; Martin, R. L.; Fox, D. J.; Keith, T.; Al-Laham, M. A.; Peng, C. Y.; Nanayakkara, A.; Challacombe, M.; Gill, P. M. W.; Johnson, B.; Chen, W.; Wong, M. W.; Gonzalez, C.; Pople, J. A. *Gaussian 03*, revision-E.01-SMP; Gaussian, Inc.: Wallingford, CT, 2004.
- (33) *Jaguar 6.0*; Schrödinger Inc.: Portland, OR, 2004.
- (34) Fernandez-Lima, F. A.; Cardozo, T. M.; Rodriguez, R. M.; Ponciano, C. R.; da Silveira, E. F.; Nascimento, M. A. C. *J. Phys. Chem.* **2007**, *A111*, 8302.
- (35) Tuma, C.; Sauer, J. *Phys. Chem. Chem. Phys.* **2006**, *8*, 3955.
- (36) Breneman, C. M.; Wiberg, K. W. *J. Comput. Chem.* **1990**, *11*, 361.
- (37) Fernandez-Lima, F. A.; Ponciano, C. R.; da Silveira, E. F.; Nascimento, M. A. C. *Chem. Phys. Lett.* **2007**, *445*, 147.
- (38) Fernandez-Lima, F. A.; Ponciano, C. R.; Nascimento, M. A. C.; da Silveira, E. F. *Chem. Phys. Lett.* **2006**, *426*, 351.
- (39) Fernandez-Lima, F. A.; Ponciano, C. R.; Faraudo, G. S.; Grivet, M.; da Silveira, E. F.; Nascimento, M. A. C. *Chem. Phys.* **2007**, *340*, 127.
- (40) Pereira, J. A. M.; Bitsensky, I. S.; da Silveira, E. F. *Int. J. Mass Spectrom. Ion Processes* **1998**, *174*, 179.
- (41) Fenzlaff, H. P.; Illenberger, E. *Int. J. Mass Spectrom. Ion Processes* **1984**, *59*, 185.
- (42) Limao-Vieira, P.; Moutinho, A. M. C.; Los, J. J. *Chem. Phys.* **2006**, *124*, 054306.
- (43) Ponciano, C. R.; Martinez, R.; Farenzena, L. S.; Homen, M. G. P.; de Brito, A. N.; Wien, K.; da Silveira, E. F. *J. Mass. Spectrom.* **2008**, *43*, 1521.
- (44) Blondel, C.; Caccioni, P.; Delsart, C.; Tranhauer, R. *Phys. Rev. A* **1989**, *40*, 3678.

JP905138D